

# Vortex Dynamics in Nonlinear Free Surface Flow

Christopher W. Curtis\*

Department of Mathematics and Statistics, San Diego State University

Henrik Kalisch†

Department of Mathematics University of Bergen

## Abstract

The motion of point vortices in an inviscid fluid with a free surface and an impenetrable bed is investigated. The work is based on forming a closed system of equations for surface variables and vortex positions using a variant of the AFM formulation [1] of the water-wave free-surface problem. The equations are approximated with a dealiased spectral method making use of a high-order approximation of the Dirichlet-Neumann operator and a high-order time-stepping scheme.

Numerical simulations reveal that the combination of vortex motion and solid bottom boundary yields interesting dynamics not seen in the case of vortex motion in an infinitely deep fluid. In particular, strong deformations of the free surface, including non-symmetric surface profiles and regions of large energy concentration are observed. Our simulations also uncover a rich variety of vortex trajectories including orbiting and nearly parallel patterns of motion. The dynamics of the free surface and of the point vortices are strongly influenced by the initial placement and polarity of the vortices.

The method put forward here is flexible enough to handle a large number of vortices, and may easily be extended to include the effects of varying bathymetry, stratification and background shear currents.

## 1 Introduction

Motivated by the need to identify moving underwater objects by their surface wave signatures, a number of authors have studied the problem of how free fluid surfaces respond to the motion of submerged vortices. This has included detailed analytic studies of one or two vortices for short times [2, 3], and numerical and experimental studies of two vortices over asymptotically significant time scales [4, 5, 6, 7]. Complementing this work, using conformal maps and asymptotic methods, the way in which an isolated vortex induces surface wave radiation up to and past the speed of sound was studied in [8]. Previous work on vortex pairs defined two types, the so-called ‘sub-critical’ and ‘super-critical’ cases characterized by the magnitude of the non-dimensional Froude number. In the super-critical case, the vortices move closer together while rising, inducing the formation of a surface hump around the vortices and ‘scars’, or depressions, on either side of the surface hump.

---

\*ccurtis@mail.sdsu.edu

†henrik.kalisch@math.uib.no

The sub-critical case is characterized by a relatively weak surface response with the vortex motion proceeding as in the case of a rigid lid for long time scales. In either case though, on long enough time scales, breaking occurs when the vortices are close enough to the surface.

However, in this previous work, the fluid is assumed infinitely deep and constraints are explicitly placed on the flow which keep the vortex positions symmetric. Thus bottom boundary effects are not captured, and while there is agreement with experimental results, the symmetry restrictions used in previous simulation and analysis do not allow for the full range of possible flows. To go further then, in a shallow-water regime, by extending the method of [1], we derive a system of differential-integral equations which describes the surface/point vortex system for an arbitrary number of submerged vortices. Using the Dirichlet-to-Neumann operator (DNO) approach of [9, 10], we are able to develop long-time numerical simulations which capture most if not all of the nonlinear interactions between the surface and the vortices, where again we can have an arbitrary number of vortices. This is a fundamentally different approach than has been used in previously in the relevant literature.

In order to connect back to previous work, we examine flows with a counter-rotating vortex pair in the fluid interior. This is done both under a traveling wave and under a quiescent surface. We study several parameter regimes in the case of vortices moving under a traveling wave which allows us to characterize sub and super critical parameter regimes. Likewise, for the case of initially quiescent surface profiles, while we are able to find much of the general phenomena seen previously, we see that waves of higher amplitude form over shorter time scales due to the presence of the bottom boundary which produces an upwelling effect unseen in previous work. This leads to the formation of large amplitude nonlinear waves with deeper scars than previously observed. Ultimately, this appears to lead to wave breaking on much faster time scales.

We then look at several cases of two pairs of vortices with net zero angular momentum. While sharing some similar characteristics with the two-vortex case, the added interactions give rise to a wide variety of higher amplitude surface profiles and potential wave-breaking mechanisms that have not been studied. While multi-vortex systems have been looked at in [11], where the canonical Hamiltonian structure of collections of vortices underneath surface waves was derived, the dynamics of multi-vortex systems were not studied. Thus our results are fundamentally new.

The study of larger collections of vortices is motivated by the experiments in [12, 13, 14] which show that surface waves induce eddy formation as they move over varying bathymetry in shallow water. The interaction between eddies and surface waves is not well studied, and as these experiments show, it appears to be an ubiquitous feature of coastal flows. We argue then that the present work is a first step towards developing a vortex based method [15], in which collections of irrotational point vortices are used to approximate larger vortical structures. As noted in [15], such methods capture the physics of the flow while allowing for the use of simple systems of model equations.

Aside from facilitating the development of numerical simulations, other effects could be readily included to the present work, such as varying bathymetry, stratification, and constant background shear currents. Further, the framework used in this paper allows for the ready derivation of asymptotic reductions of the full nonlinear system, thus providing further physical insight that would be difficult to obtain from direct simulation alone. Developing these ideas may lead to a better understanding of tsunami propagation and wave-energy device design, and thus the present work should have impact on important applications.

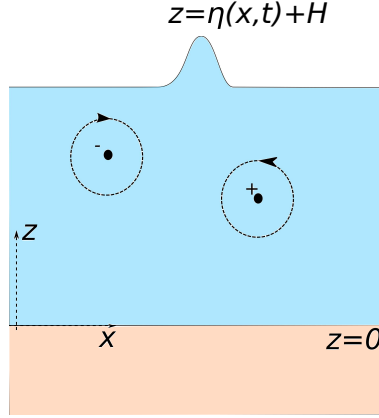


Figure 1: Irrotational point vortices submerged under a free surface gravity wave.

The outline of the paper is as follows. The remainder of this section presents the classic, bulk-variable dependent model for the surface-wave/vortex system. Section 2 presents the extension to the method in [1] whereby we write model equations in terms of surface variables and vortex positions alone, thus removing any dependence on bulk-variables. Section 3 presents the shallow water formulation of the surface-wave/vortex system. DNO expansions and the linearization of the surface -wave/vortex system are derived. Section 4 presents the results of several numerical simulations involving both two and four vortices. Section 5 presents conclusions of this work and also further describes future directions.

### 1.1 Model Formulation

Throughout this work, we assume the fluid is inviscid and incompressible. We place an impermeable boundary at  $z = 0$  and a free surface at  $z = \eta(x, t) + H$ . The only vorticity in the problem comes from a collection of irrotational point vortices submerged beneath the free surface. We take the fluid domain to be periodic, with period  $2L$ , and  $-L \leq x \leq L$ . See Figure 1 for reference.

Given our assumptions on the fluid, the fluid velocity  $\mathbf{u}$  is given by the gradient of a potential, say  $\phi$ . We can further separate this potential by writing

$$\phi(x, z, t) = \phi_v(x, z, t) + \tilde{\phi}(x, z, t).$$

The potential  $\tilde{\phi}$  describes the bulk and surface fluid flow while the potential describing the vortex motion,  $\phi_v$ , is defined to be

$$\phi_v(x, z, t) = \frac{1}{2\pi} \sum_{j=1}^N \Gamma_j \phi_{v,j}(x, z, t), \quad (1)$$

with  $\Gamma_j$  denoting the circulation strength of the vortices and

$$\phi_{v,j}(x, z, t) = \phi_{v,j}^+(x, z, t) - \phi_{v,j}^-(x, z, t),$$

where, denoting the vortex positions as  $\mathbf{x}_j(t) = (x_j(t), z_j(t))$ , we set

$$\phi_{v,j}^+(x, z, t) = \Phi_p(x - x_j(t), z - z_j(t)), \quad \phi_{v,j}^-(x, z, t) = \Phi_p(x - x_j(t), z + z_j(t)),$$

where

$$\Phi_p(x, z) = \sum_{m=-\infty}^{\infty} \tan^{-1} \left( \frac{z}{x - 2mL} \right).$$

Our choice for  $\phi_v$ , aside from addressing the requirement of periodic boundary conditions, ensures that

$$\partial_z \phi_v|_{z=0} = 0.$$

By further supposing that

$$\partial_z \tilde{\phi} \Big|_{z=0} = 0,$$

we satisfy the assumption that  $z = 0$  is an impermeable boundary.

Standard arguments then give for the vortex velocities

$$\dot{x}_j = \frac{1}{4L} \left( \Gamma_j \coth \left( \frac{\pi z_j}{L} \right) + 2 \sum_{l \neq j} \Gamma_l v_{jl}^{(h)} \right) + \tilde{\phi}_x(x_j, z_j, t), \quad (2)$$

$$\dot{z}_j = \frac{1}{2L} \sinh \left( \frac{\pi}{L} z_j \right) \sum_{l \neq j} \Gamma_l v_{jl}^{(v)} + \tilde{\phi}_z(x_j, z_j, t), \quad (3)$$

where

$$v_{jl}^{(h)} = \frac{\sinh \left( \frac{\pi}{L} z_l \right) \left( \cosh \left( \frac{\pi}{L} z_l \right) - \cosh \left( \frac{\pi}{L} z_j \right) \cos \left( \frac{\pi}{L} (x_j - x_l) \right) \right)}{\left( \cosh \left( \frac{\pi}{L} (z_j - z_l) \right) - \cos \left( \frac{\pi}{L} (x_j - x_l) \right) \right) \left( \cosh \left( \frac{\pi}{L} (z_j + z_l) \right) - \cos \left( \frac{\pi}{L} (x_j - x_l) \right) \right)},$$

$$v_{jl}^{(v)} = \frac{\sin \left( \frac{\pi}{L} (x_j - x_l) \right) \sinh \left( \frac{\pi}{L} z_l \right)}{\left( \cosh \left( \frac{\pi}{L} (z_j - z_l) \right) - \cos \left( \frac{\pi}{L} (x_j - x_l) \right) \right) \left( \cosh \left( \frac{\pi}{L} (z_j + z_l) \right) - \cos \left( \frac{\pi}{L} (x_j - x_l) \right) \right)}.$$

At the surface, we have the kinematic condition which, separating into vortex and bulk variables becomes

$$\eta_t - \tilde{\phi}_z + \eta_x \tilde{\phi}_x = P_v(x, \eta, t), \quad z = \eta(x, t) + H, \quad (4)$$

where

$$P_v(x, \eta, t) = \partial_z \phi_v - \eta_x \partial_x \phi_v.$$

Finally, at the surface, we have the Bernoulli equation, which becomes after separating into vortex and bulk variables

$$\tilde{\phi}_t + \frac{1}{2} \left| \nabla \tilde{\phi} \right|^2 + \nabla \phi_v \cdot \nabla \tilde{\phi} + g\eta = E_v(x, \eta, t), \quad (5)$$

where

$$E_v(x, \eta, t) = \frac{1}{2\pi} \sum_{j=1}^N \Gamma_j \left( \dot{x}_j \partial_x \phi_{v,j} + \dot{z}_j \partial_z \left( \phi_{v,j}^+ + \phi_{v,j}^- \right) \right) - \frac{1}{2} |\nabla \phi_v|^2.$$

The system given by Equations (2)-(5) coupled with the bulk requirement that

$$\Delta \tilde{\phi} = 0, \quad 0 \leq z \leq \eta(x, t) + H, \quad (6)$$

and the Neumann boundary condition  $\partial_z \tilde{\phi}(x, 0, t) = 0$ , gives a closed system of equations in terms of  $\eta$ ,  $\tilde{\phi}$ , and the vortex positions  $(x_j(t), z_j(t))$ . However, this requires the solution of a nonlinear

free boundary value problem, which does not allow for any direct analytic solution approaches. Further, even with regards to developing numerical schemes, any method which removes the need to solve throughout the bulk of the fluid is desirable. This goal can be at least partially achieved by defining

$$\tilde{q}(x, t) = \tilde{\phi}(x, \eta(x, t) + H, t),$$

we can transform the derivatives of the potential at the surface via the equations

$$\begin{pmatrix} \tilde{\phi}_x \\ \tilde{\phi}_z \end{pmatrix} \Big|_{z=\eta+H} = \frac{1}{1+\eta_x^2} \begin{pmatrix} 1 & \eta_x \\ \eta_x & -1 \end{pmatrix} \begin{pmatrix} \tilde{q}_x \\ -\eta_t + P_v \end{pmatrix}, \quad (7)$$

and

$$\tilde{\phi}_t = \tilde{q}_t - \tilde{\phi}_z \eta_t, \quad (8)$$

and therefore rewrite the Bernoulli equation (5) in terms of surface variables and vortex positions alone. However, since we have made use of the kinematic condition Equation (4), we cannot rewrite this equation in terms of itself. Likewise, we have no means of removing the bulk-variable dependence in Equations (2) and (3).

To address this issue, we now turn to the method of Ablowitz, Fokas, and Mussilmani (AFM) as described in [1]. Through an extension to the existing scheme, we will be able to write a closed system of equations in terms of surface variables and vortex positions alone. This will remove any need to solve equations, either analytically or numerically, throughout the bulk of the fluid. As we show, this approach then readily allows us to derive efficient numerical approximation schemes.

## 2 The Surface-Variable/Vortex-Position Formulation

We now show how to rewrite the system of equations (2)-(6) in terms of surface variables and vortex positions alone via the method described in [1]. Making use of Equation (4), the work in [1] readily allows us to rewrite the kinematic condition as the infinite system of integro-differential equations

$$\int_{-L}^L e^{-i\pi kx/L} (\cosh(k(\eta + H)) (\eta_t - P_v) + i\tilde{q}_x \sinh(k(\eta + H))) dx = 0, \quad (9)$$

for  $k \in \mathbb{Z} \setminus \{0\}$ . We omit the details of this derivation since one may directly follow the arguments in [1] to derive (9).

Looking at Equations (2) and (3) though, we are still left with needing to evaluate the background flow potential  $\tilde{\phi}$  at the vortex positions  $(x_j, z_j)$ . To deal with this, we introduce the auxillary harmonic functions

$$\psi_j(x, z, t) = -\frac{1}{4\pi} \sum_{m=-\infty}^{\infty} (\ln(\tilde{x}_{j,m}^2 + \tilde{z}_{j,-}^2) + \ln(\tilde{x}_{j,m}^2 + \tilde{z}_{j,+}^2)).$$

where

$$\tilde{x}_{j,m} = \frac{(x - x_j - 2mL)}{L}, \quad \tilde{z}_{j,-} = \frac{\gamma}{H}(z - z_j), \quad \tilde{z}_{j,+} = \frac{\gamma}{H}(z + z_j),$$

and

$$\gamma = \frac{H}{L}.$$

We are then able to show the identity

$$\tilde{\phi}_x(x_j, z_j, t) = - \int_{-L}^L \left( \tilde{\phi}_z (\partial_x \psi_j + \eta_x \partial_z \psi_j) + \tilde{\phi}_x (-\eta_x \partial_x \psi_j + \partial_z \psi_j) \right) \Big|_{z=\eta+H} dx,$$

See the Appendix, Section 6.1, for the technical details of the derivation. Using the kinematic condition and basic definitions then allows us to show that

$$\tilde{\phi}_x(x_j, z_j, t) = - \int_{-L}^L ((\eta_t - P_v) \partial_x \psi_j + \tilde{q}_x \partial_z \psi_j) \Big|_{z=\eta+H} dx. \quad (10)$$

Proceeding in a similar fashion for  $\tilde{\phi}_z$ , we introduce the auxillary harmonic function

$$\tilde{\psi}_j = -\frac{1}{4\pi} \sum_{m=-\infty}^{\infty} (\ln(\tilde{x}_{j,m}^2 + \tilde{z}_{j,-}^2) - \ln(\tilde{x}_{j,m}^2 + \tilde{z}_{j,+}^2)).$$

This choice ensures that  $\tilde{\psi}_j(x, 0, t) = 0$ . Again, using the arguments described in the Appendix, Section 6.1, we then can find that

$$\tilde{\phi}_z(x_j, z_j, t) = - \int_{-L}^L \left( \tilde{\psi}_j (\eta_x \tilde{\phi}_{xz} + \tilde{\phi}_{xx}) + \tilde{\phi}_z (-\eta_x \partial_x \tilde{\psi}_j + \partial_z \tilde{\psi}_j) \right) \Big|_{z=\eta+H} dx,$$

where we have used the fact that  $\tilde{\phi}_{zz} = -\tilde{\phi}_{xx}$ . Integrating by parts then gives

$$\tilde{\phi}_z(x_j, z_j, t) = - \int_{-L}^L \left( -\tilde{\phi}_x (\partial_x \tilde{\psi}_j + \eta_x \partial_z \tilde{\psi}_j) + \tilde{\phi}_z (-\eta_x \partial_x \tilde{\psi}_j + \partial_z \tilde{\psi}_j) \right) \Big|_{z=\eta+H} dx,$$

which can be shown, again using Equation (7), to yield

$$\tilde{\phi}_z(x_j, z_j, t) = - \int_{-L}^L ((\eta_t - P_v) \partial_z \tilde{\psi}_j - \tilde{q}_x \partial_x \tilde{\psi}_j) \Big|_{z=\eta+H} dx.$$

Thus, we have now shown how to rewrite Equations (2) and (3) in the bulk-independent form

$$\begin{aligned} \dot{x}_j = & \frac{1}{4L} \left( \Gamma_j \coth \left( \frac{\pi z_j}{L} \right) + 2 \sum_{l \neq j} \Gamma_l v_{jl}^{(h)} \right) \\ & - \int_{-L}^L ((\eta_t - P_v) \partial_x \psi_j + \tilde{q}_x \partial_z \psi_j) \Big|_{z=\eta+H} dx, \end{aligned} \quad (11)$$

$$\begin{aligned} \dot{z}_j = & \frac{1}{2L} \sinh \left( \frac{\pi}{L} z_j \right) \sum_{l \neq j} \Gamma_l v_{jl}^{(v)} \\ & - \int_{-L}^L ((\eta_t - P_v) \partial_z \tilde{\psi}_j - \tilde{q}_x \partial_x \tilde{\psi}_j) \Big|_{z=\eta+H} dx. \end{aligned} \quad (12)$$

Thus, coupled with the use of (7) to rewrite (5), and the use of the AFM method to derive (9), we have now derived a system of equations that are in terms of surface variables and vortex positions alone.

### 3 Shallow Water Theory: Scalings and Linear Dynamics

We now choose the following non-dimesionalizations

$$\tilde{x} = \frac{x}{L}, \quad \tilde{z} = \frac{z}{H}, \quad \tilde{t} = \frac{\sqrt{gH}}{L}t, \quad \eta = d\tilde{\eta}, \quad \tilde{\phi} = \mu L \sqrt{gH} \tilde{\tilde{\phi}},$$

where we define the non-dimensional parameters

$$\mu = \frac{d}{H}, \quad \gamma = \frac{H}{L},$$

and where we define the *global* Froude number  $F$  to be

$$F = \frac{\Gamma}{\mu L \sqrt{gH}}.$$

Following [2], we also define the *local* Froude number  $F_{loc}(t)$  to be

$$F_{loc}(t) = \frac{\Gamma}{D(t)} \frac{1}{\sqrt{g(H + \eta(x_m(t), t))}}, \quad D(t) = |z_m(t) - (H + \eta(x_m(t), t))|,$$

where

$$z_m(t) = \max_{1 \leq j \leq n} z_j(t),$$

and  $x_m(t)$  is the horizontal coordinate corresponding to  $z_m(t)$ . Thus,  $F_{loc}$  measures the relative magnitudes of the surface wave velocity to the velocity induced by the vortex. We note that after non-dimensionalization and dropping tildes, the local Froude number becomes

$$F_{loc}(t) = \frac{\mu F}{\gamma} \frac{1}{|z_m(t) - (1 + \mu \eta(x_m(t), t))| \sqrt{1 + \mu \eta(x_m(t), t)}}.$$

Thus we see that  $F_{loc}$  is determined by the key non-dimensional parameters of the model.

If we then define  $Q = \tilde{q}_x$ , the Bernoulli equation (5) becomes, after using Equations (7) and (8) and then dropping tildes,

$$Q_t + \eta_x + \mu \partial_x \frac{1}{1 + \mu^2 \gamma^2 \eta_x^2} \left( \frac{1}{2} Q^2 - \mu \gamma^2 \eta_t \eta_x Q + \phi_{sx} (Q + \mu \gamma \eta_x (P_s - \gamma \eta_t)) \right. \\ \left. + \frac{1}{2} (P_s^2 - \gamma^2 \eta_t^2) + \phi_{sz} (\gamma \mu \eta_x Q - (P_s - \gamma \eta_t)) \right) = \partial_x E_s(x, t), \quad (13)$$

where

$$P_s(x, t) = \phi_{sz}(x, t) - \mu \gamma \eta_x \phi_{sx}(x, t),$$

and

$$E_s(x, t) = F \sum_{j=1}^N \Gamma_j (\dot{x}_j \varphi_x(x - x_j, 1 + \mu \eta; z_j) + \gamma \dot{z}_j \tilde{\varphi}_z(x - x_j, 1 + \mu \eta; z_j)) - \frac{\mu}{2} (\phi_{sx}^2 + \phi_{sz}^2).$$

The AFM equation (9) becomes

$$\int_{-1}^1 e^{-i\pi kx} \left( \cosh(\pi\gamma k(1 + \mu\eta)) \left( \eta_t - \frac{1}{\gamma} P_v(x, 1 + \mu\eta, t) \right) + i \frac{1}{\gamma} Q \sinh(\pi\gamma k(1 + \mu\eta)) \right) dx = 0, \quad k \in \mathbb{Z}, \quad (14)$$

and Equations (11) and (12) become

$$\dot{x}_j = \frac{F\mu}{4} \left( \Gamma_j \coth(\pi\gamma z_j) + 2 \sum_{l \neq j} \Gamma_l v_{jl}^{(h)} \right) + \quad (15)$$

$$\mu \int_{-1}^1 ((\gamma\eta_t - P_s) \tilde{\varphi}_z(x - x_j, z; z_j) + Q \tilde{\varphi}_x(x - x_j, z; z_j))|_{z=1+\mu\eta} dx, \\ \dot{z}_j = \frac{F\mu}{2\gamma} \sinh(\pi\gamma z_j) \sum_{l \neq j} \Gamma_l v_{jl}^{(v)} - \quad (16)$$

$$\frac{\mu}{\gamma} \int_{-1}^1 ((\gamma\eta_t - P_s) \varphi_x(x - x_j, z; z_j) + Q \varphi_z(x - x_j, z; z_j))|_{z=1+\mu\eta} dx,$$

The definitions of  $\phi_{sx}$ ,  $\phi_{sz}$ ,  $\varphi_x$ ,  $\varphi_z$ ,  $\tilde{\varphi}_x$ , and  $\tilde{\varphi}_z$  can be found in the Appendix, Section 6.2,. We now develop the machinery necessary to implement numerical schemes to solve the system of equations (13), (14), (15), and (16).

### 3.1 Dirichlet-to-Neumann Expansions

Our choice of scaling allows us to readily generate the Dirichlet-to-Neumann Operator (DNO) expansion. This is done, as in [9] and elsewhere, by supposing that

$$\eta_t - \frac{1}{\gamma} P_v(x, 1 + \mu\eta, t) = (G_0 + \mu G_1 + \mu^2 G_2 + \dots) Q.$$

Defining the Fourier transform of a periodic function  $f(x)$  to be  $\hat{f}$ , so that

$$\hat{f}(k) = \frac{1}{2} \int_{-1}^1 f(x) e^{-i\pi kx} dx, \quad k \in \mathbb{Z},$$

we define, for a linear operator  $L$ , its associated symbol  $\hat{L}(k)$  by way of the formula

$$\hat{L}(k) \hat{f}(k) = \frac{1}{2} \int_{-1}^1 L f(x) e^{-i\pi kx} dx.$$

Using the AFM equation (14), we then get

$$\hat{G}_0(k) = -\frac{i}{\gamma} \tanh(\pi\gamma k),$$



and, for  $m \geq 1$ ,

$$G_m Q = - \sum_{j=1}^{\lfloor m/2 \rfloor} \frac{1}{(2j)!} D_\gamma^{2j} (\eta^{2j} G_{m-2j} Q) \\ - \gamma^2 \partial_x G_0 \sum_{j=0}^{\lfloor (m-1)/2 \rfloor} \frac{D_\gamma^{2j}}{(2j+1)!} (\eta^{2j+1} G_{m-2j-1} Q) - \frac{1}{m!} L_m \partial_x D_\gamma^{m-1} (\eta^m Q),$$

where

$$\hat{D}_\gamma = \pi \gamma k,$$

and

$$\hat{L}_m = \begin{cases} 1, & m \text{ is odd,} \\ i\gamma \hat{G}_0(k), & m \text{ is even.} \end{cases}$$

### 3.2 Linear Dynamics

In order to get at least some short time intuition about the response of the above system, we suppose that  $\mu \ll \gamma$ , so that in the linear regime we have  $\dot{x}_j \sim 0$ ,  $\dot{z}_j \sim 0$ ,

$$Q_t + \eta_x = 0,$$

and

$$\hat{\eta}_t - \hat{G}_0(k) \hat{Q} = F \int_{\mathbb{R}} e^{-i\pi k x} \tilde{P}_v dx,$$

where

$$\tilde{P}_v = \frac{\gamma \sqrt{2}}{\pi} \sum_{j=1}^n \Gamma_j z_j e^{-i\pi k x_j} \frac{x}{(x^2 + \gamma^2(1 - z_j)^2)(x^2 + \gamma^2(1 + z_j)^2)}.$$

We can readily show using a contour integral argument that

$$\int_{\mathbb{R}} e^{-i\pi k x} \tilde{P}_v dx = -\frac{i}{\sqrt{2}} \sum_{j=1}^n \Gamma_j \frac{\sinh(\pi \gamma k z_j)}{\gamma} e^{-i\pi k x_j - \pi \gamma |k|}.$$

Note, in order for this result to hold, we need to assume that  $0 \leq z_j < 1$ . Thus, if we linearize around a quiescent initial condition, using (1) whereby we have

$$\hat{\eta}(k, 0) = 0, \quad \hat{Q}(k, 0) = \hat{Q}_0(k) = -ik \hat{\phi}_v(k, 1)$$

in frequency space, we get the leading order behavior

$$\begin{pmatrix} \hat{Q}(k, t) \\ \hat{\eta}(k, t) \end{pmatrix} = \hat{Q}_0(k) \begin{pmatrix} \cos(\omega(k)t) \\ \frac{\omega}{i\pi k} \sin(\omega(k)t) \end{pmatrix} \\ - \frac{iF}{\sqrt{2}} \begin{pmatrix} i\pi k (\cos(\omega(k)t) - 1)/\omega(k) \\ \sin(\omega(k)t) \end{pmatrix} \sum_{j=1}^n \Gamma_j \frac{\sinh(\pi \gamma k z_j)}{\gamma \omega(k)} e^{-i\pi k x_j - \pi \gamma |k|},$$

where

$$\omega(k) = \sqrt{\frac{\pi k \tanh(\pi \gamma k)}{\gamma}}.$$

Defining the surface response to the vortex induced forcing as  $R_s(x, t)$ , we readily see that this is given by

$$R_s(x, t) = F \sum_{j=1}^n \Gamma_j R_{s,j}(x, t).$$

where the functions  $R_{s,j}$  are found by taking inverse Fourier transforms and using symmetry arguments such that one finds

$$R_{s,j}(x, t) = \sum_{k=1}^{\infty} \frac{\sin(\omega(k)t)}{\omega(k)} \frac{\sinh(\pi \gamma k z_j)}{\gamma} e^{-\pi \gamma k} \sin(\pi k(x - x_j)). \quad (17)$$

### 3.3 Shallow Water Regime

By setting the vortex strengths to zero, we would expect to recover the classical case of shallow water flow in which the KdV equation becomes a valid asymptotic approximation. Expanding up to  $\mathcal{O}(\mu, \gamma^2)$  we get the system of equations

$$Q_t + \eta_x + \frac{\mu}{2} \partial_x Q^2 \sim 0,$$

and

$$\left(1 - \frac{\gamma^2}{2} \partial_x^2\right) \eta_t + \partial_x \left(1 - \frac{\gamma^2}{6} \partial_x^2\right) Q + \mu \partial_x (\eta Q) \sim 0.$$

By introducing the coordinates

$$\xi = x - t, \quad \tau = \mu t,$$

and taking the balance

$$\gamma = \sqrt{\mu},$$

we derive the Korteweg-de Vries (KdV) equation

$$2Q_\tau + 3QQ_\xi + \frac{1}{3}Q_{\xi\xi\xi} = 0.$$

Note, we see by deriving this equation that we are in fact, in the absence of vortices, in a classically defined shallow water regime, thus justifying our choice of scalings *a posteriori*.

As is known, the KdV equation has an infinite number of periodic traveling wave solutions of the form

$$Q(x, t) \sim \frac{2}{3}q_0 + \frac{4}{3}\tilde{m}^2 \mathcal{K}^2(\tilde{m}) \text{cn}^2(\mathcal{K}(\tilde{m})(x - (1 + \mu\tilde{c})t); \tilde{m}), \quad (18)$$

where

$$\tilde{c} = \frac{2}{3}\mathcal{K}^2(\tilde{m})(2\tilde{m}^2 - 1) + q_0,$$

and where  $0 \leq \tilde{m} < 1$  is the elliptic modulus of the cnoidal function  $\text{cn}(\cdot; \tilde{m})$  and where  $\mathcal{K}(\tilde{m})$  represents the complete elliptic integral of the first kind. This then implies that the surface profile is to leading order given by

$$\eta(x, t) \sim \left(1 + \frac{2}{3}\mu\mathcal{K}^2(\tilde{m})(2\tilde{m}^2 - 1)\right) Q(x, t). \quad (19)$$

We will study the interactions between these profiles and vortices in the following section.

### 3.4 Convergence of the method for $F = 0$

In order to test our numerical method and the formulation of the problem, we take  $F = 0$  and use initial conditions corresponding to the choice  $t = 0$  in the solutions to the KdV Equation given by Equations (18) and (19) with  $\tilde{m} = .2$  and  $q_0$  chosen so that the initial conditions have zero spatial average. While KdV solutions are not exact, we provide a Cauchy convergence study of our method to establish its validity throughout the remainder of the paper. For all of the following simulations, we use a pseudo-spectral in space and fourth order Runge-Kutta in time method of lines. The time step used is  $\delta t = 1 \times 10^{-2}$ , and the error introduced by these choices is on the order of  $10^{-8}$ .

The chief concern with regards to numerical accuracy in using DNO expansions comes from issues related to the catastrophic cancellation of the higher order terms [17]. To see this, we first choose  $\mu = .2$  and  $\gamma = \sqrt{\mu}$ . We choose  $K_M = 256$  and  $K_M = 512$ , and we truncate the DNO expansion at the 11th term, i.e.  $G_{10}$ , for both choices of total number of modes. Letting the simulation run to  $t_f = 12$ , we see in Figure 2 that the two solutions for  $\eta(x, 12)$  are indistinguishable up to machine precision. We note that this result has nothing to do with the validity of KdV as an approximation to the full problem. We therefore see over an asymptotically significant time scale, i.e.  $t_f > 2/\mu$ , that the method has converged.

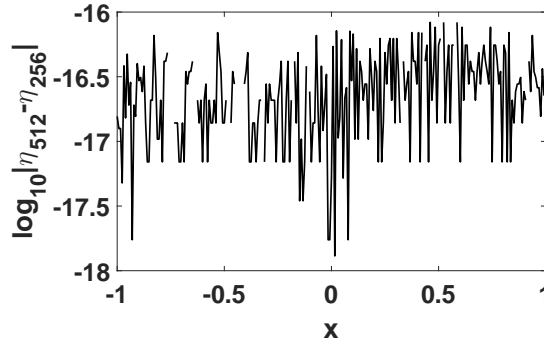


Figure 2: Log plot of the difference in the solutions at  $t_f = 12$  using  $K_M = 256$  and  $K_M = 512$  modes. As can be seen, the solutions are identical up to machine precision, and thus the sampling rate described in the introduction should be sufficient. Here  $\mu = .2$  and  $\gamma = \sqrt{\mu}$ .

In contrast, we now choose  $\mu = .4$  while still letting  $\gamma = \sqrt{\mu}$ . Again letting  $t_f = 12$ , we compare the performance of the method by looking at the difference between using  $K_M = 64$  and  $K_M = 128$  modes and then using  $K_M = 256$  and  $K_M = 512$  modes. We double the number of terms used in the DNO expansion by truncating at the 21st mode, i.e.  $G_{20}$ . As seen in Figure 3, while one can

argue that using  $K_M = 512$  modes still produces a very accurate solution, the combination of the larger value of  $\mu$  and  $\gamma$  has allowed for the catastrophic cancellation described in [17] to begin to drive errors up in comparison to using simulations with lower numbers of modes. To further make

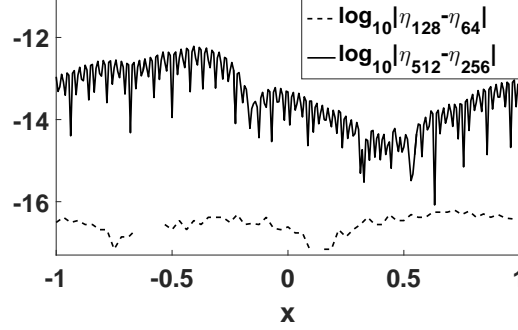


Figure 3: Log plot of the difference in the solutions at  $t_f = 12$  using  $K_M = 64$  and  $K_M = 128$  modes (- -) and using  $K_M = 256$  and  $K_M = 512$  modes (-). As can be seen, the introduction of higher modes allows catastrophic cancellation to remove two digits of relative accuracy. Here  $\mu = .4$  and  $\gamma = \sqrt{\mu}$ .

the point, we can reduce the magnitude of the long wave parameter  $\gamma$  such that  $\gamma = \mu = .4$ . In this case, as we see in Figure 4, while catastrophic cancellation issues still keep the simulations with  $K_M = 512$  modes as accurate as lower mode simulations, this effect is greatly mitigated by having reduced the magnitude of the long wavelength parameter  $\gamma$ .

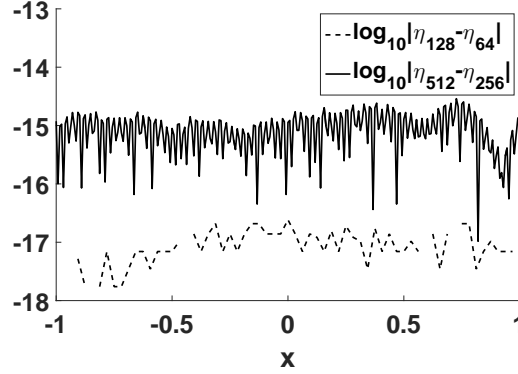


Figure 4: Log plot of the difference in the solutions at  $t_f = 12$  using  $K_M = 64$  and  $K_M = 128$  modes (- -) and using  $K_M = 256$  and  $K_M = 512$  modes (-). As can be seen, while catastrophic cancellation still plays a role, by decreasing the magnitude of  $\gamma$ , it is significantly mitigated. Here  $\mu = .4$  and  $\gamma = \mu$ .

## 4 Numerical Results

We now describe the general details of our numerical experiments involving different vortex configurations. Throughout the remainder of the paper, while our choice for  $\mu$  will vary, we choose  $\gamma = \sqrt{\mu}$  since this corresponds to the KdV balance described above and is a typical choice for “shallow-water” models. From the convergence studies above, we likewise sample the domain with  $K_M = 512$  modes so that the wavenumbers  $k$  satisfy  $-255 \leq k \leq 256$ . In order to avoid aliasing, the Orszag “2/3-rule” is used throughout the simulations. Thus, since the non-dimensional domain is  $[-1, 1]$ , this choice corresponds to a grid spacing of  $\delta x \approx .006$ .

For the problems involving only two vortices, we use the initial positions

$$\begin{aligned} x_1(0) &= -\mu\gamma, \quad z_2(0) = 0.25, \\ x_2(0) &= +\mu\gamma, \quad z_1(0) = 0.25. \end{aligned}$$

This is done since  $d/L = \mu\gamma$ , and thus these initial positions are equivalent to assuming that the separation length between the vortices is of the same order as the characteristic wave amplitude. For those problems involving four vortices, we use two different sets of starting positions. The first clusters the vortices so that

$$\begin{aligned} x_1(0) &= -2\mu\gamma - \mu\gamma/2, \\ x_2(0) &= -2\mu\gamma + \mu\gamma/2, \\ x_3(0) &= 2\mu\gamma - \mu\gamma/2, \\ x_4(0) &= 2\mu\gamma + \mu\gamma/2. \end{aligned}$$

Thus each vortex is within  $\mu\gamma$  of its nearest neighbor. In the second set, we space the vortices evenly so that

$$\begin{aligned} x_1(0) &= -3\mu\gamma/2, \\ x_2(0) &= -\mu\gamma/2, \\ x_3(0) &= \mu\gamma/2, \\ x_4(0) &= 3\mu\gamma/2. \end{aligned}$$

In all cases we start with  $z_j(0) = 0.25$ . Throughout, we keep  $|\Gamma_j| = 1$  and use the Froude number  $F$  to set the effective strength of the vortices.

It is nontrivial at this point to describe what choices of  $F$  correspond to subcritical or supercritical vortices as described in the previous literature. We note that our choice of  $F$  is not the same as in for example [2] or [6], where they define the Froude number  $\tilde{F}$  to be

$$\tilde{F} = \frac{\Gamma}{d^{3/2}g^{1/2}}.$$

Comparing these two choices of Froude number shows our choice for  $F$  satisfies the equation

$$F = \gamma\sqrt{\mu}\tilde{F}.$$

The supercritical or strong case is usually taken to be when  $\tilde{F} \geq 1$ , which corresponds to  $F \geq 0.2$  using the values for  $\mu$  and  $\gamma$  from above. However, the distinction between subcritical and supercritical is more succinctly defined using a phenomenological approach, whereby in the subcritical case, the motion of surface waves has a strong influence on vortex motion, and in the supercritical case, the vortex motion drives surface wave dynamics. We explore this issue in detail throughout the remaining sections.

For each simulation, there is of course the question of where to truncate the DNO expansions. We use the convention of taking enough terms, say  $\tilde{N}$ , such that, using the numerically computed solution for  $Q(x, t_f)$ , where  $t_f$  is the final time a given simulation is run to, we satisfy the criteria

$$\frac{\|G_{\tilde{N}}Q\|_2}{\|Q\|_2} \leq \text{eps},$$

where eps denotes machine precision, which on 64-bit machines is on the order of  $10^{-16}$ . We argue that satisfying this inequality should in most cases imply subsequent terms should have little to no effect on the dynamics. However, throughout each simulation, multiple truncation points were chosen to see what impact they had on dynamics, and in all cases, no effect was seen by including terms beyond what would be selected via our truncation convention.

This argument though of course relies on the choice of  $t_f$ . Throughout each simulation,  $t_f$  is chosen to be long enough so that nonlinear effects can become asymptotically significant, but not long enough so that arbitrarily high-frequency effects dominate the dynamics. As each simulation shows, and as we would expect, these high-frequency modes are due to vortices getting closer to the free surface. We can think of the corresponding high-frequency phenomena as a loss in regularity of the surface profile, which is to say that the surface profile is starting to break. This is a heuristic measurement, and more sophisticated simulations, such as vortex sheet based methods [6, 16], would need to be done to establish at what times vertical gradients or singularities in the wave profile formed. That breaking could occur is not surprising, and breaking has been observed in the deep water simulations reported on previously [5].

To get some quantitative understanding of when breaking might occur, and to get a better understanding of how moving vortices impart energy into the surface, we include plots of the surface energy  $E(t)$  defined to be

$$E(t) = \frac{1}{2} \int_{-1}^1 qG(\eta)Qdx + \frac{1}{2} \int_{-1}^1 \eta^2 dx.$$

We again note that  $Q = q_x$ , and our use of  $Q$  implies that the form of the DNO  $G$  is different than that found in for example [9]. As shown in [11], the surface-wave/vortex system is Hamiltonian with total energy given by  $E(t)$  and the energy possessed by the vortices themselves. Thus  $E(t)$  provides a direct measurement of the balance between the energy in the surface and the vortices, and we use the dynamics of  $E(t)$  to describe when we think breaking phenomena begin to occur.

#### 4.1 Two Counter Propagating Vortices under a Traveling Wave

Choosing the elliptic modulus to be  $\tilde{m} = 0.2$ , we look at the case of two counter-propagating vortices under the traveling wave where we compare the dynamics for  $F = 0, 0.02$ , and  $0.2$ . In all cases, we truncate the DNO expansion at the 32nd term, i.e.  $G_{31}$ . We run each simulation

up to  $t = 5 = 1/\mu$  so that nonlinear effects have time to become asymptotically significant. We then choose  $q_0 = 0$  so that as  $\tilde{m} \rightarrow 1$ , we limit onto the classical one-soliton solution of the KdV equation.

We note that the case  $F = 0$  is equivalent to setting the vortex strengths to zero and thus represents the path of passive tracers in the bulk of the fluid. As can be seen then from the motion of the vortices in Figure 5, there is very little difference between the vortex paths for  $F = 0.02$  and the path of a passive tracer. Likewise, observing the surface response seen in Figure 6, we see the vortex motion has little to no effect on the surface wave profile. Thus, we can readily argue that the choice of  $F = 0.02$  corresponds to a sub-critical value of the Froude number. In contrast, the choice of  $F = 0.2$  clearly corresponds to a super-critical choice. This can be seen in the stronger vortex dynamics in Figure 5 as well as the significant impact the vortices have on the surface profile in Figure 7 which induces significant deformations of the original cnoidal profile.

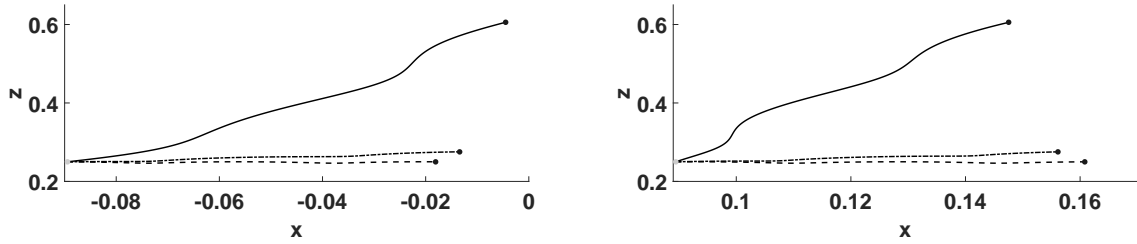


Figure 5: Trajectories of the right-side vortex moving under a cnoidal wave for  $0 \leq t \leq 5$  for Froude numbers  $F = 0$  (dashed line),  $0.02$  (dashed/dotted line), and  $0.2$  (solid line). The vortex motion starts at the light grey dot and ends at the black dot.

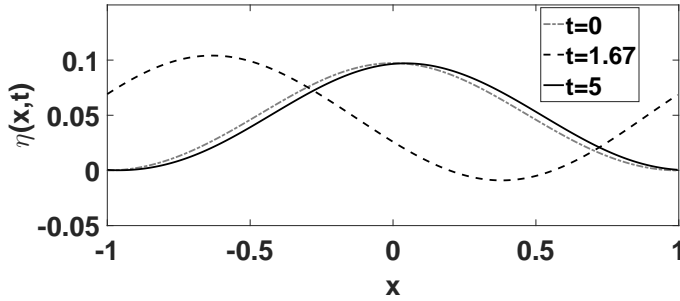


Figure 6: Surface response  $\eta(x, 5)$  for a traveling cnoidal solution of the KdV equation with elliptic modulus  $\tilde{m} = 0.2$  and Froude number  $F = 0.02$ .

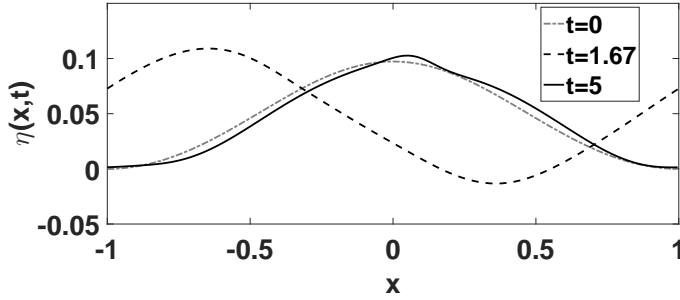


Figure 7: Surface response  $\eta(x, 5)$  for a traveling cnoidal solution of the KdV equation with elliptic modulus  $\tilde{m} = 0.2$  and Froude number  $F = 0.2$ .

## 4.2 Two Counter Propagating Vortices Under an Initially Quiescent Surface

Throughout the remainder of the paper, use the initial conditions

$$\eta(x, 0) = 0, \quad Q(x, 0) = -\partial_x \phi_v(x, 1),$$

so that the initial surface profile is flat and still. On relatively short time scales, we can compare our numerics to the linear theory derived in the previous section. Using Equation (17), we can show that for a pair of counter-rotating vortices, the forcing response for the free surface is given by the function

$$R_s(x, t) = 2 \sum_{k=1}^{\infty} \frac{\sin(\omega(k)t)}{\omega(k)} \frac{\sinh(\pi\gamma k z_1)}{\gamma} e^{-\pi\gamma k} \sin(\pi k x_1) \cos(\pi k x). \quad (20)$$

We note that this result relies on assuming the vortices are essentially stationary. We expect though that as the vortices rise, there will be a limited time scale over which the linear theory is valid. To quantify this, we define the time  $t_l$  which is the first time  $t$  at which

$$\frac{\|\eta(\cdot, t) - R_s(\cdot, t)\|_2}{\|\eta(\cdot, t)\|_2} \geq \mu$$

For  $t \geq t_l$ , we expect nonlinear effects to become significant due to the rise of the vortex pair.

In the particular case for  $F = .2$  at  $t = .5$ , we see in Figure 8 that the linear response is quite accurate. Further, the falling troughs, or scars, seen in much of the existing literature [5, 7] are present. However, we note that in previous work, the formation of mounds in the surface profile corresponded to the vortices being near the wave crest. Thus, the presence of the bottom boundary and the concomitant upwelling it induces causes wave profiles to form at far shorter time scales and for different reasons than reported in previous literature.

In order to study the impact of changing  $F$  and  $\mu$ , we plot  $t_l$  as a function of  $F$  for  $.1 \leq F \leq .3$  in the cases  $\mu = .1$  and  $\mu = .2$ ; see the lower panel of Figure 8. This figure displays several fascinating qualities. First, perhaps somewhat surprisingly, the break down in the linear theory happens more quickly for the smaller choice of  $\mu$ , i.e. when  $\mu = .1$ . Thus, the smaller value of  $\mu$  allows for a more rapid movement of the vortices which drives the system away from the linear limit. What is



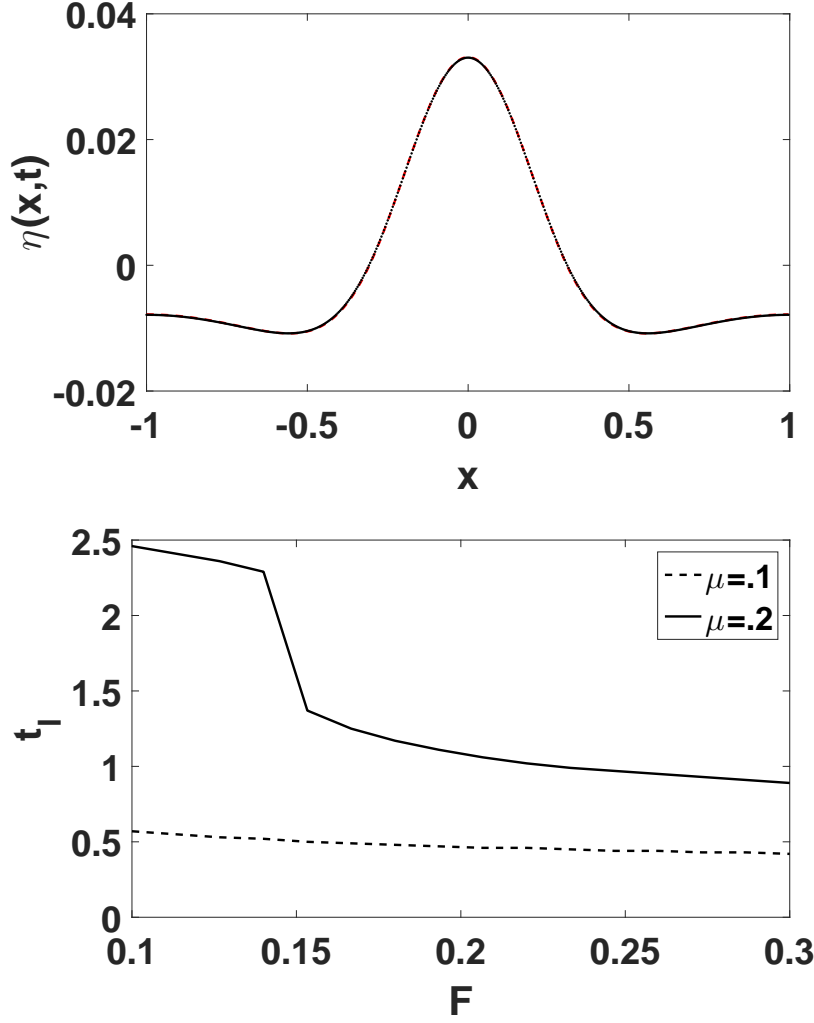


Figure 8: Comparison between linear theory ( $\cdot$ ) and numerics ( $-$ ) at  $t = 0.5$  (upper panel) and  $t_l$  as a function of  $F$  (lower panel). For  $\mu = .2$ , there is a rapid transition in the time at which nonlinearity becomes significant around  $F = .15$  (lower panel).

especially striking though is rapid transition in  $t_l$  for  $\mu = .2$  near  $F = .15$ . The significant decrease in  $t_l$  at this Froude number gives a possible indication of the difference between sub and super critical choices of the Froude number. The super critical case then corresponds to a faster onset time of nonlinear effects. What is also provocative though is that this result only seems to hold for  $\mu = .2$ . For  $\mu = .1$  there is no significant change in  $t_l$  for varying Froude number. Therefore the difference between sub and super critical behavior could be highly parameter dependant.

To further explore the role of nonlinearity then, we now look at longer timescales where we let time  $t = 9 \sim 45F$ . We truncate the DNO expansions at the 18th term, i.e.  $G_{17}$ . As seen in Figure 9, comparing the surface profiles at  $t = 3, 6$ , and  $9$ , higher frequency phenomena and distinguished peaks form as the vortices rise. Looking at the power spectra at  $t = 9$  in Figure 11, we see that a

significant amount of energy has been transported into higher wave numbers as the vortices rise. As seen in Figure 9 (lower panel), as the vortices rise, the amount of energy shared between the surface and the vortices stays relatively constant up to about  $t = 4$ . But once high enough, the vortices begin to pump energy into the surface at a greater rate as seen near  $t = 9$ .

Simulations over longer time scales show that after  $t = 9$ , the numerical method breaks down with the appearance of ever higher frequency oscillations, which suggests that the wave is physically near breaking. See also Figure 11, where one sees that while high-frequency modes are still at relatively low energies, the surface profile is no longer well sampled. The appearance of these high frequency modes corresponds to a sharp rise in the total surface energy as seen in Figure 10. However, again presumably due to the bottom boundary, as seen in Figure 9 (lower panel), this breaking occurs even though the vortices are still well separated from the surface. Further, we see that the vortices reflect away from the surface near  $t = 9$ , reminiscent of vortex motion in inviscid wall bounded flow [18].

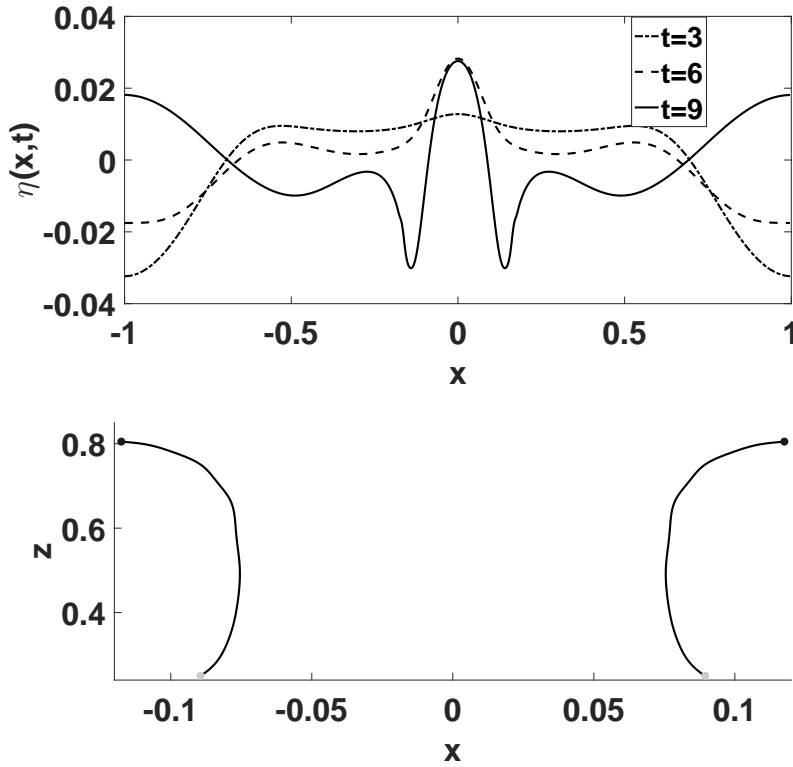


Figure 9: Upper panel: Surface response  $\eta(x, t)$  at  $t = 3$ ,  $t = 6$ , and  $t = 9$  over two counter-propagating vortices for  $F = .2$ . Lower panel: Motion of the two counter-propagating vortices for  $0 \leq t \leq 9$ . The light grey dots indicate where the vortices begin and the black dots indicate their positions at  $t = 9$ .

A question we can then ask is how the choice of Froude number influences the time of onset of breaking. Taking the number of modes in the pseudo-spectral scheme to be  $K_M = 512$ , using the 2/3-rule means the highest effective mode in the numerical scheme is  $k_* = 170$ . We then define the

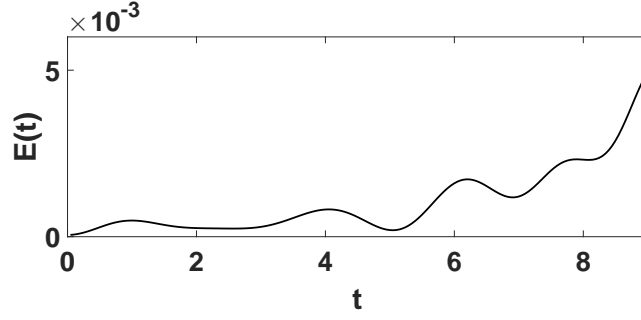


Figure 10: Surface energy profile  $E(t)$  for a surface over two vortices for  $0 \leq t \leq 9$  for  $F = .2$ .

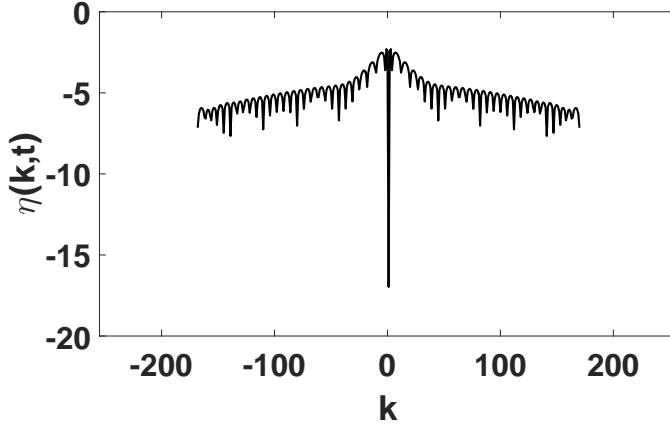


Figure 11: Log plot of the power spectrum of the free surface  $\eta$  at  $t = 9$  over wave numbers  $-255 \leq k \leq 256$  for  $F = .2$ . As the counter-propagating vortices rise, they pump more energy into higher wavenumbers of the initially flat surface.

breaking time  $t_b$  to be that time such that

$$|\hat{\eta}_{k_*}| = 10^{-9}.$$

As noted above, since we cannot model overturning waves, this should be taken as a rough measure, though we argue that once so much energy has appeared in such high wavenumbers, this is a reasonable measure of when a wave would begin forming vertical gradients. In conjunction with this, we also look at the local Froude number at  $t_b$  divided by the global Froude number  $F$ ,  $F_{loc}(t_b)/F$ .

As seen in Figure 12, and as one would expect, increasing the Froude number increases the speed with which vortices rise and impart energy into the surface and then induce breaking. This relationship is clearly nonlinear also nonlinear for both  $\mu = .1$  and  $\mu = .2$ . Again, we emphasize that we take  $\gamma = \sqrt{\mu}$  in both cases. Again, as with the computation of  $t_l$ , the smaller value of the wave amplitude parameter  $\mu = .1$  allows for the vortices to rise faster and thus induce breaking more rapidly than in the case where  $\mu = .2$ . A possible explanation for this is for fixed Froude number  $F$ , the amount of energy in the vortices is the same, but the energy barrier to surface

deformation in the  $\mu = .1$  case is lower than for  $\mu = .2$ . Thus there is less resistance to the rise of the vortices, allowing them to surface faster and induce breaking in the surface.

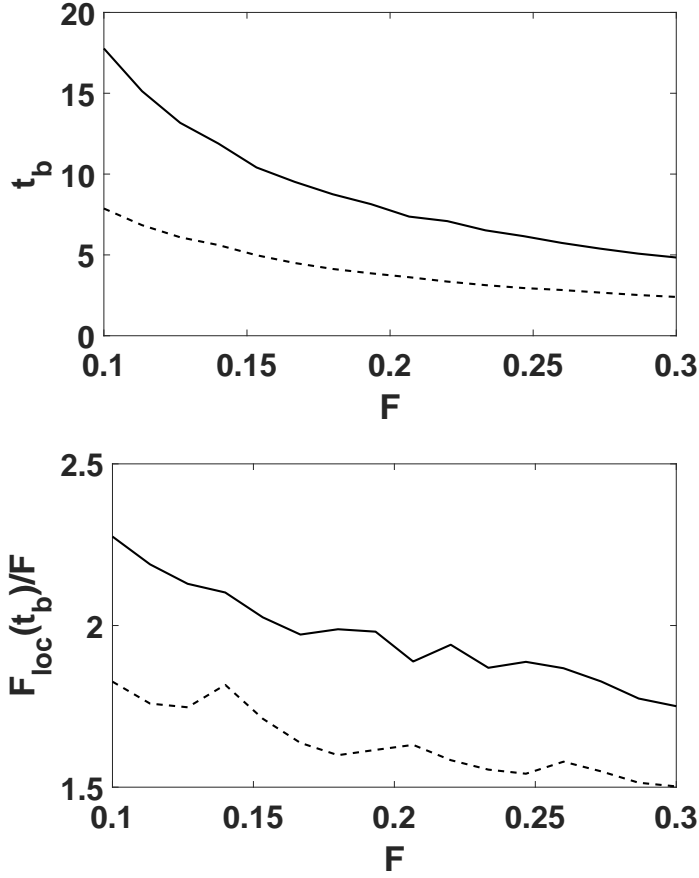


Figure 12: Plot of the breaking time  $t_b$  (upper panel) and local Froude number  $F_{loc}(t_b)$  (lower panel) as a function of Froude number  $F$  for small amplitude values  $\mu = .1$  (- -) and  $\mu = .2$  (-). While the smaller parameter value  $\mu = .1$  allows for a faster rise of the vortices and thus an earlier onset of breaking (upper panel), the point at which we see surface breaking must happen within an  $\mathcal{O}(\sqrt{\mu})$  thick layer of the surface (lower panel).

### 4.3 Four Propagating Vortices: Plus/Plus, Minus/Minus

Using the same numerical scheme and parameters as from above, we now look at the case of four vortices, chosen with vortex strengths

$$\Gamma_1 = \Gamma_2 = 1, \Gamma_3 = \Gamma_4 = -1.$$

We refer to this choice of vortex strengths as the ‘Plus/Plus, Minus/Minus’ (PPMM) case. We study this for both the asymmetric (APPMM) and symmetric (SPPMM) initial vortex configurations. Looking at the particular case of  $F = 0.2$ , we compare the dynamics of the surface response,

vortex paths, and energy exchange of the APPMM and SPPMM configurations in Figures 13-15 respectively. Both the APPMM and SPPMM cases give us our first sense of how one might simulate underwater eddies beneath free surface waves.

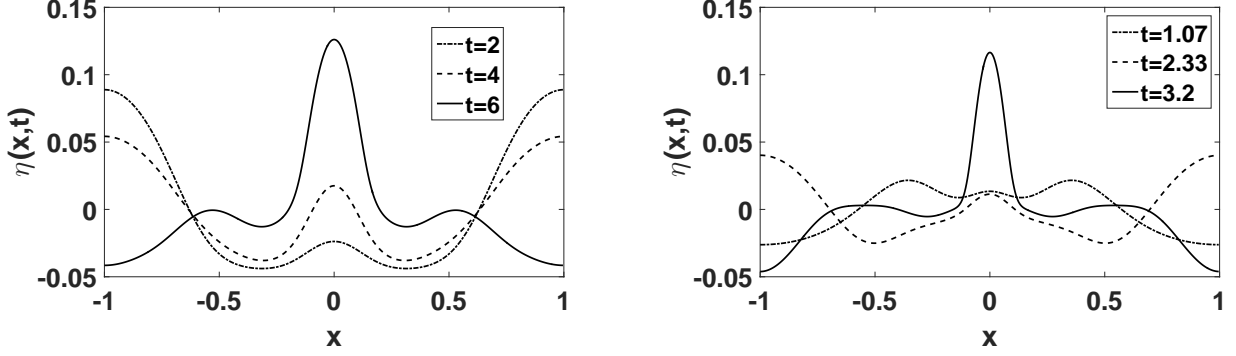


Figure 13: Left panel: Surface response  $\eta(x, t)$  over four vortices in the asymmetric PPMM configuration. Right panel: Surface response  $\eta(x, t)$  over four vortices in the SPPMM configuration.

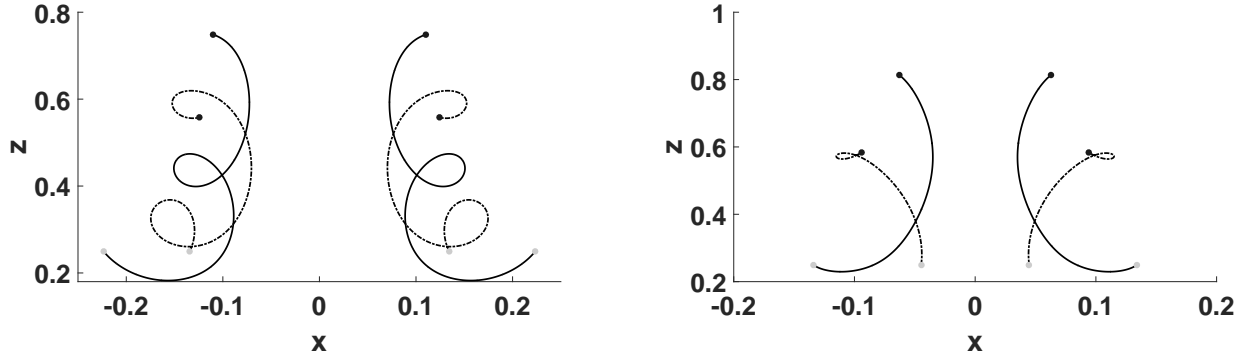


Figure 14: Left panel: Vortex paths for four vortices in the APPMM configuration. Right panel: Vortex paths for four vortices in the SPPMM configuration.

#### 4.4 Four Propagating Vortices: Plus/Minus, Minus/Plus

We now examine the case of four vortices with vortex strengths chosen such that

$$\Gamma_1 = 1, \Gamma_2 = -1, \Gamma_3 = -1, \Gamma_4 = 1,$$

which is why we refer to this case as ‘Plus/Minus, Minus/Plus’ or PMMP. We choose  $F = 0.2$ . The simulation can be run to  $t = 4$  before high frequency phenomena causes the numerical method to break down. As seen in Figure 17, the surface profile is highly asymmetric. Likewise, it is clear that the peak in Figure 17 is due to the presence of the leftmost vortex pair as seen in Figure 17 (lower panel). The vortex pair on the right side travels down, where it behaves as in inviscid wall-bounded flows [18].

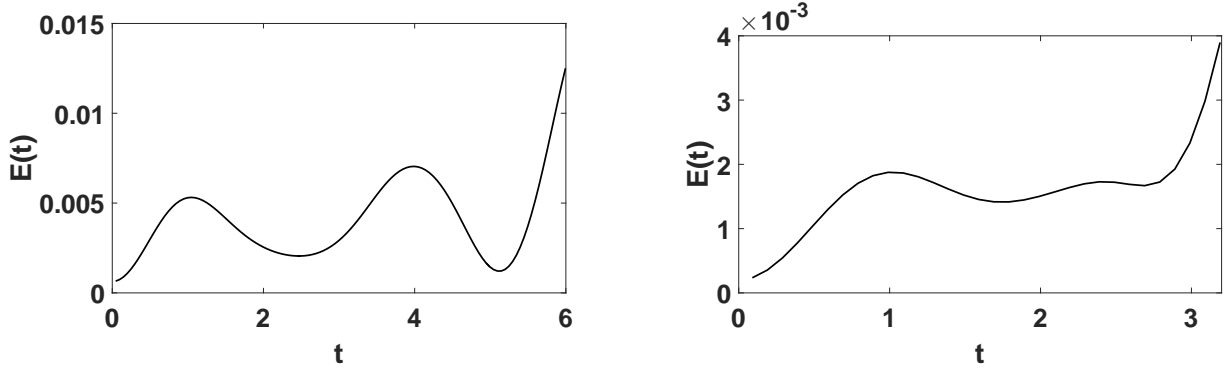


Figure 15: Surface energy profile  $E(t)$  in response to the motion of four vortices in the APPMM configuration (left panel) and SPPMM configuration (right panel).

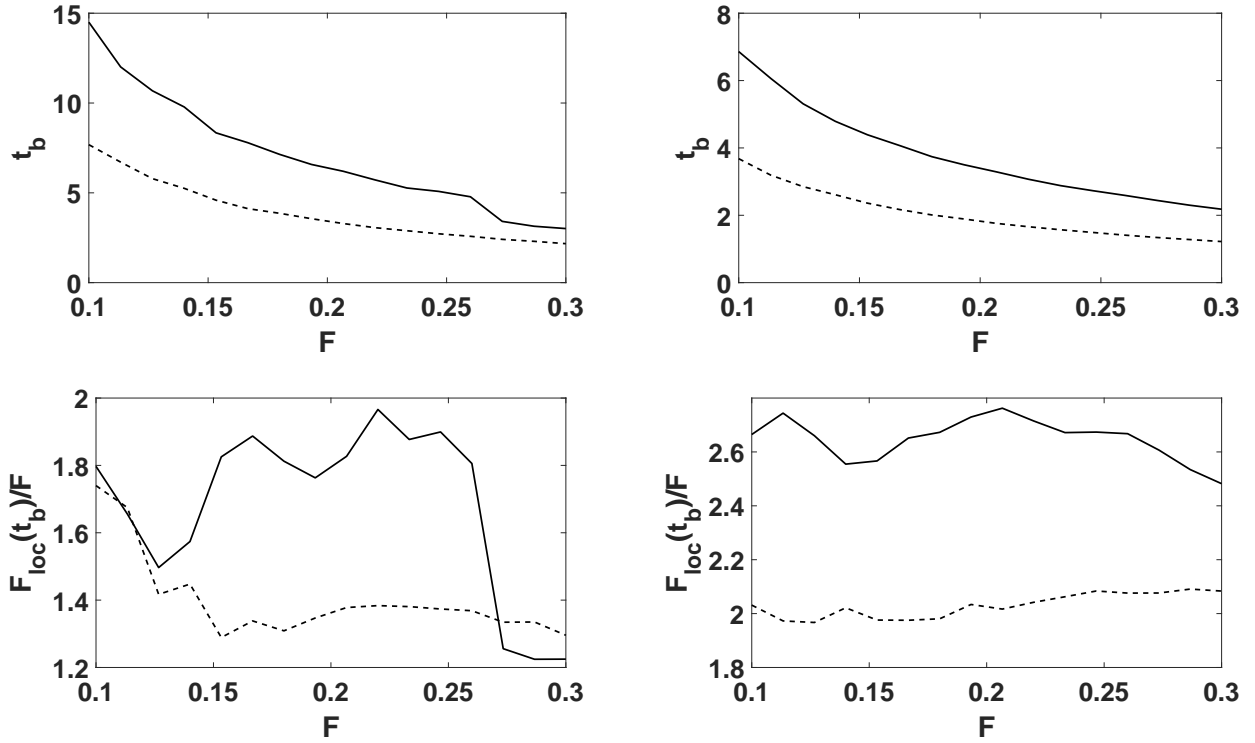


Figure 16: Plot of the breaking time  $t_b$  (upper panels) and ratio of the local Froude number to the global Froude number  $F_{loc}(t_b)/F$  (lower panels) as a function of Froude number  $F$  for amplitude values  $\mu = .1$  ( - - ) and  $\mu = .2$  ( - ) for four vortices in the APPMM configuration (left panels) and the SPPMM configuration (right panels). While the smaller parameter value  $\mu = .1$  allows for a faster rise of the vortices and thus an earlier onset of breaking (upper panel).

#### 4.5 Four Propagating Vortices: Plus/Minus, Plus/Minus

Finally, we now look at the case of four vortices, chosen so that

$$\Gamma_1 = 1, \Gamma_2 = -1, \Gamma_3 = 1, \Gamma_4 = -1.$$

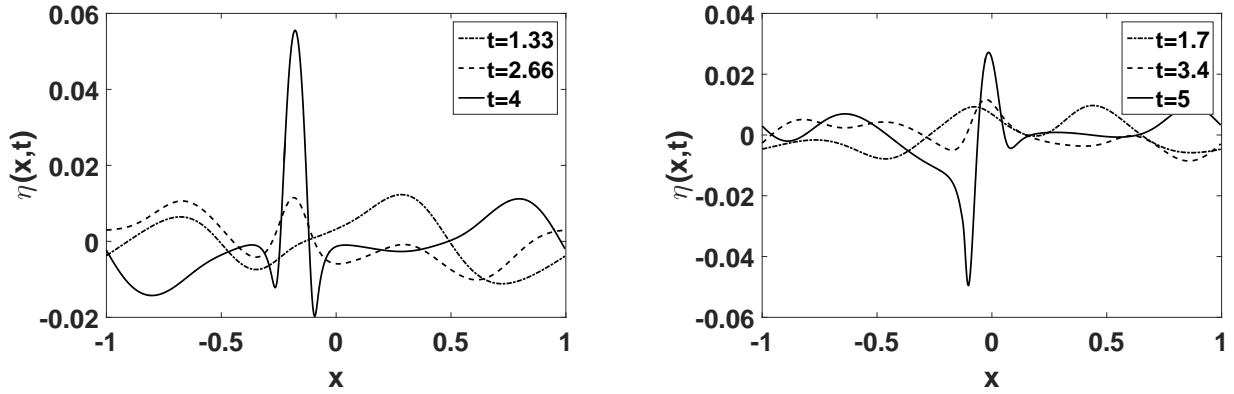


Figure 17: Left panel: Surface response  $\eta(x,t)$  over four vortices in the APMMP configuration. Right panel: Surface response  $\eta(x,t)$  over four vortices in the SPMMP configuration.

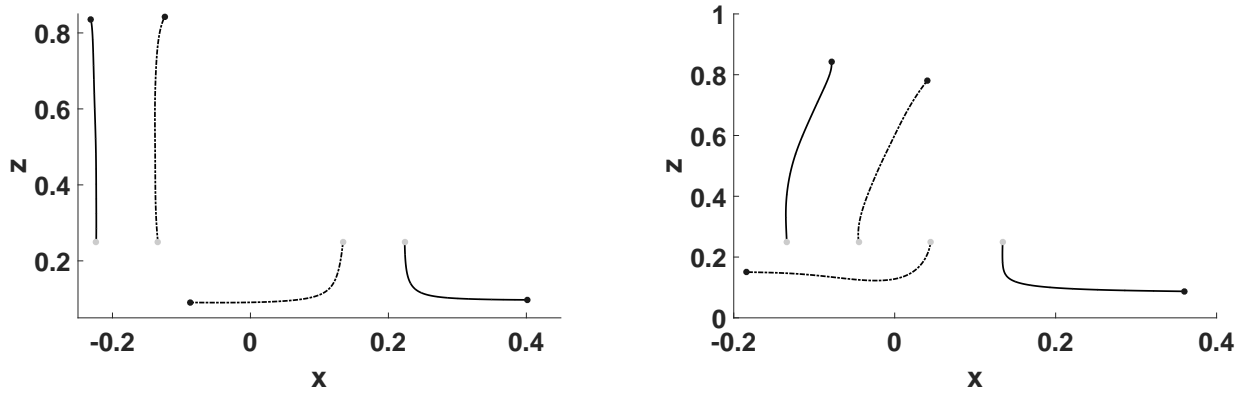


Figure 18: Left panel: Vortex paths for four vortices in the APMMP configuration. Right panel: Vortex paths for four vortices in the SPMMP configuration.

The Froude number is again set at  $F = 0.2$ . In keeping with our convention, this is called the ‘Plus/Minus,Plus/Minus’ case. The simulation can be run to  $t = 4$  before high frequency phenomena causes the numerical method to break down. The flow breaks the symmetry of the vortices in the vertical direction, as seen in Figure ?? (lower panel). Likewise, this case produces perhaps the most distinct and complicated surface profile as seen in the upper panel of Figure ?. Again, the appearance of this more complicated surface profile corresponds to an increased rate of energy input from the motion of the vortices as seen in Figure 23.

## 5 Conclusions and Future Work

In this paper, we have derived a nonlinear integro-differential system of equations in terms of surface variables and vortex positions alone which allows for the ready development of numerical simulations and asymptotic approximations. While being able to recreate known results for two counter-

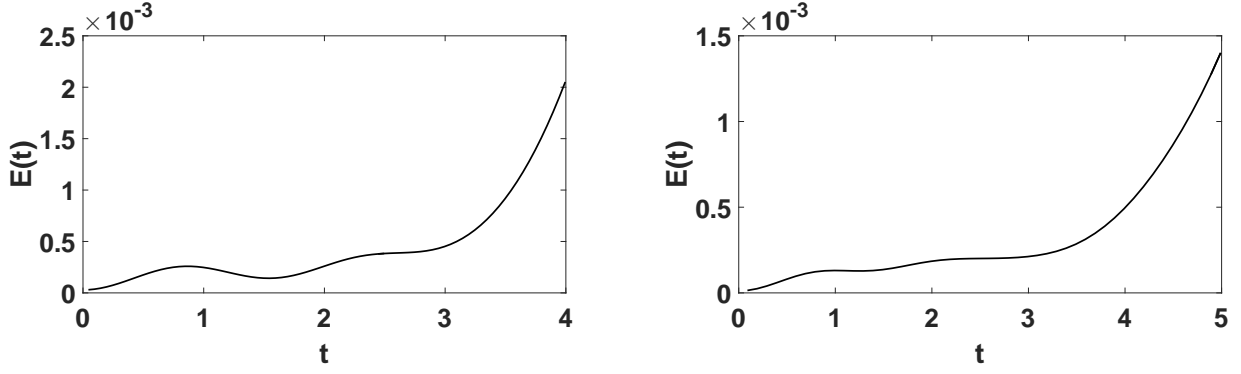


Figure 19: Surface energy profile  $E(t)$  in response to the motion of four vortices in the APMMP (left panel) and SPMMP (right panel) configurations.

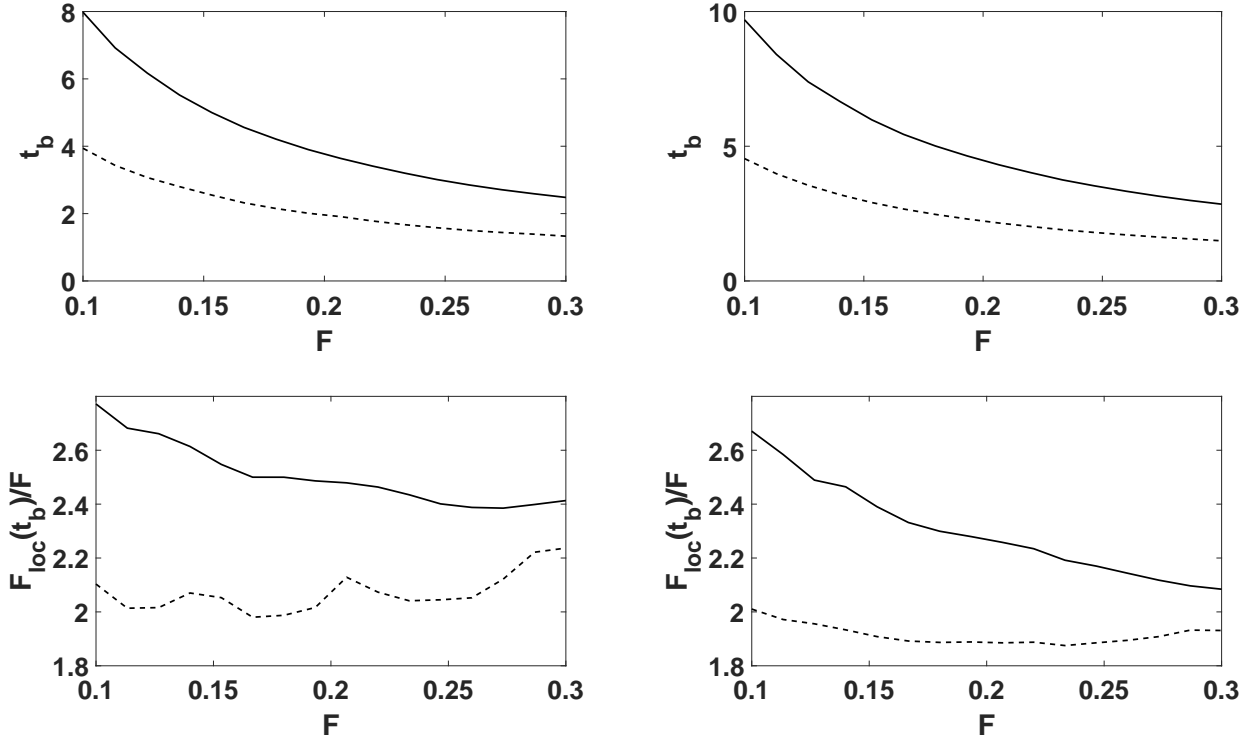


Figure 20: Plot of the breaking time  $t_b$  (upper panels) and ratio of the local Froude number to the global Froude number  $F_{loc}(t_b)/F$  (lower panels) as a function of Froude number  $F$  for amplitude values  $\mu = .1$  (- -) and  $\mu = .2$  (-) for four vortices in the APMMP (left panels) and SPMMP (right panels) configurations. The smaller parameter value  $\mu = .1$  allows for a faster rise of the vortices and thus an earlier onset of breaking (upper panel).

propagating vortices, our approach allows for arbitrary, non-symmetric vortex configurations to



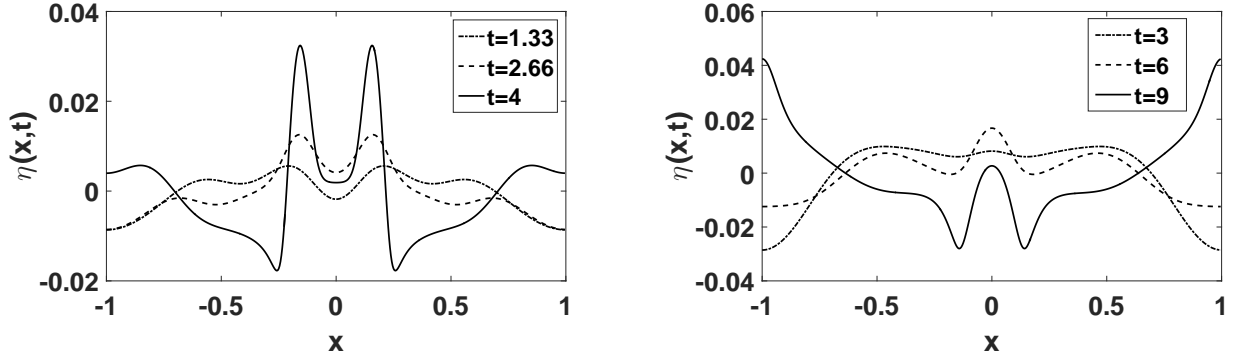


Figure 21: Left panel: Surface response  $\eta(x,t)$  for  $t = 2, 4$ , and  $6$  over four vortices in the asymmetric Plus/Plus, Minus/Minus configuration. Right panel: Surface response  $\eta(x,t)$  for  $t = 1.07, 2.33$ , and  $3.2$  over four vortices in the symmetric Plus/Plus, Minus/Minus configuration.

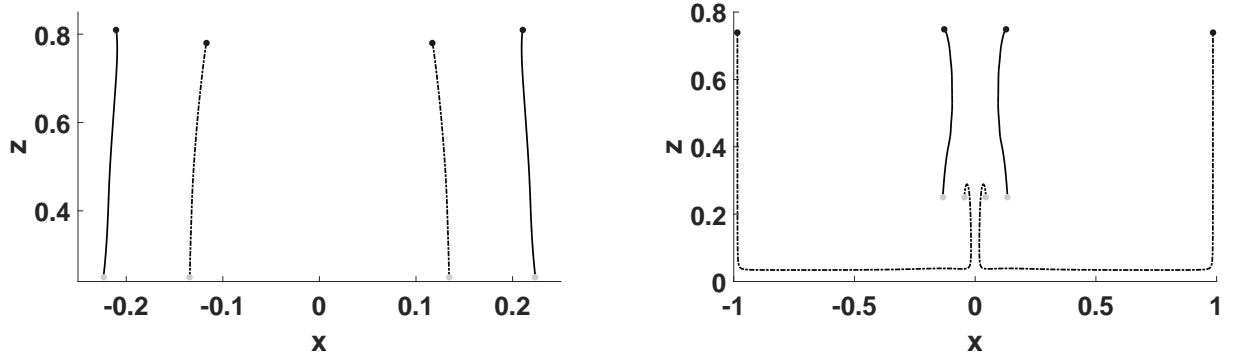


Figure 22: Left panel: Vortex paths for four vortices in the asymmetric Plus/Plus, Minus/Minus configuration. Right panel: Vortex paths for four vortices in the symmetric Plus/Plus, Minus/Minus configuration.

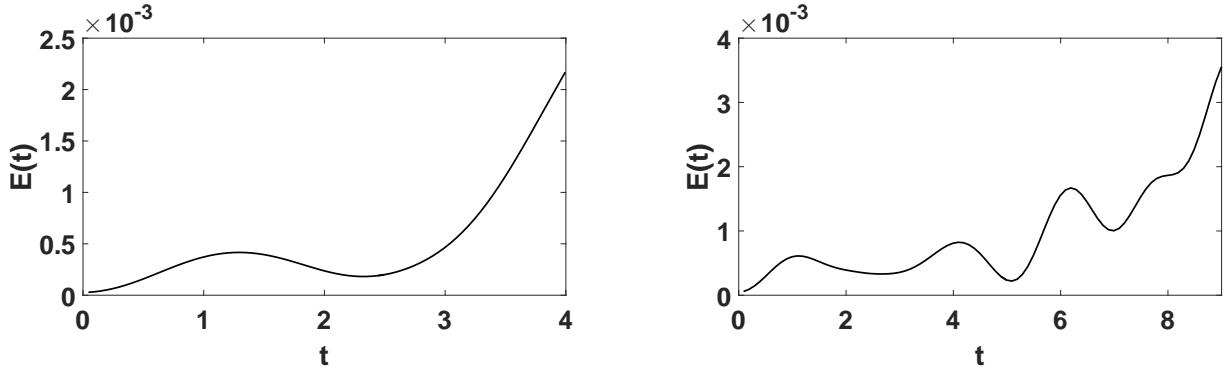


Figure 23: Surface energy profile  $E(t)$  in response to the motion of four vortices in the Plus/Plus, Minus/Minus configuration for  $0 \leq t \leq 6$ .

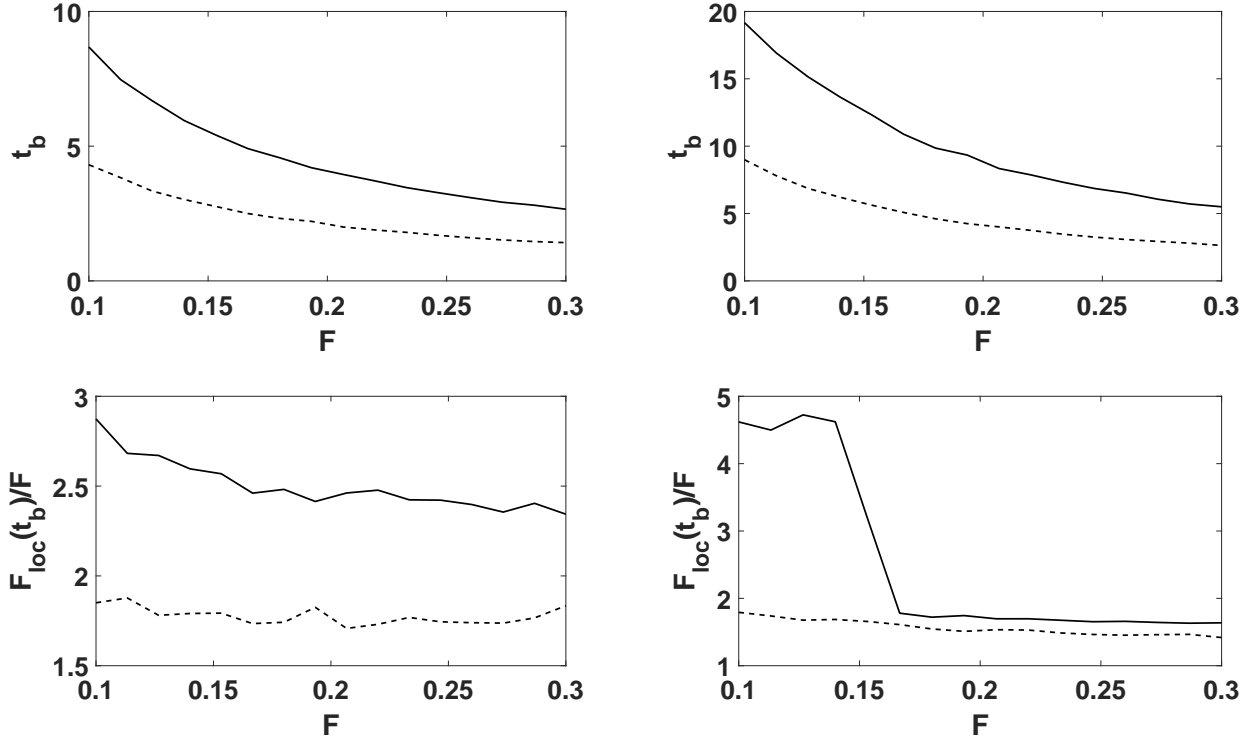


Figure 24: Plot of the breaking time  $t_b$  (upper panels) and ratio of the local Froude number to the global Froude number  $F_{loc}(t_b)/F$  (lower panels) as a function of Froude number  $F$  for amplitude values  $\mu = .1$  ( - - ) and  $\mu = .2$  ( - ) for four vortices in the Plus/Minus/Plus/Minus configuration for the asymmetric (left panels) and symmetric (right panels) case. While the smaller parameter value  $\mu = .1$  allows for a faster rise of the vortices and thus an earlier onset of breaking (upper panel), the point at which we see surface breaking must happen within an  $\mathcal{O}(\sqrt{\mu})$  thick layer of the surface (lower panel), though this is more true in the case of symmetric (right panel) than asymmetric (left panel) initial vortex placement.

be simulated which also take into account the influence of bottom boundaries of the fluid. The presence of bottom boundaries was shown to strongly influence dynamics, leading for example to breaking like phenomena on much shorter time scales than previously reported for deep water flows.

Further, since we allow for more complicated, asymmetric vortex motion, more complicated, and in particular asymmetric, surface profiles were observed. In particular, it was found that the arrangement vortices of positive and negative strength has a major effect on the dynamics of both the free surface and the motion of the vortices. For instance, in the Plus/Plus, Minus/Minus configuration shown in Figure 13, the identical sense of rotation amplifies the vorticity of the individual vortices, and the vortices are tracing out orbiting trajectories as the rise to near the surface. While the free surface stays symmetric in this case, in the Plus/Minus, Minus/Plus configuration, the surface profile becomes strongly asymmetric after a relatively short time. Finally, in the Plus/Minus, Plus/Minus configuration, the vorticity of these pairs seems to be equalized, leading to near linear vortex trajectories and symmetric surface profiles such as shown in Figure ??

The simulation of interactions between surface waves and eddies in more complicated fluid environments is a direction of future work which will build on the results in this paper.

## 6 Appendix

### 6.1 Derivation of Bulk-Potential Equation

To derive Equation (10), in order to have well-defined integrands, we first use the auxillary harmonic function

$$\psi_{M,j}(x, z, t) = -\frac{1}{4\pi} \sum_{m=-M}^M (\ln(\tilde{x}_{j,m}^2 + \tilde{z}_{j,-}^2) + \ln(\tilde{x}_{j,m}^2 + \tilde{z}_{j,+}^2)).$$

Our choice of auxillary harmonic function ensures that  $\partial_z \psi_{M,j}(x, 0, t) = 0$ , while avoiding the analytic issues of whether the above sum converges as  $M \rightarrow \infty$ . Taking  $D$  to be the fluid domain and using Green's third identity, we have that

$$\tilde{\phi}_x(x_j, z_j, t) = \oint_{\partial D} (\psi_{M,j} \partial_{\hat{\mathbf{n}}} \tilde{\phi}_x - \tilde{\phi}_x \partial_{\hat{\mathbf{n}}} \psi_{M,j}) ds,$$

where  $\hat{\mathbf{n}}$  is an outward pointing unit normal vector along the path  $\partial D_\epsilon$ . Note, if  $\tilde{\phi}$  is harmonic, then so are all of its partial derivatives. Defining

$$g_M(x, z, t) = \psi_{M,j} \partial_{\hat{\mathbf{n}}} \tilde{\phi}_x - \tilde{\phi}_x \partial_{\hat{\mathbf{n}}} \psi_{M,j},$$

We can then decompose the line integral such that

$$\begin{aligned} \oint_{\partial D} g_M(x, z, t) ds &= \int_{-L}^L g_M(x, \eta(x, t) + H, t) (1 + \eta_x^2)^{1/2} dx \\ &\quad + \int_0^{\eta(L, t) + H} (g_M(L, z, t) + g_M(-L, z, t)) dz. \end{aligned}$$

We now look at letting  $M \rightarrow \infty$ . As defined,  $\psi_{M,j}$  does not have a well defined limit, however, its derivatives are well defined in this limit, and as we show, it is well behaved along boundaries. To see this, along  $z = \eta(x, t) + H$ , we have that

$$g_M(1 + \eta_x^2)^{1/2} = \left( \psi_{M,j} (-\eta_x \tilde{\phi}_{xx} + \tilde{\phi}_{xz}) - \tilde{\phi}_x (-\eta_x \partial_x \psi_{M,j} + \partial_z \psi_{M,j}) \right) \Big|_{z=\eta+H}.$$

Using  $\tilde{\phi}_{xx} = -\tilde{\phi}_{zz}$ , we get the identity

$$\partial_x (\tilde{\phi}_z(x, \eta + H, t)) = -\eta_x \tilde{\phi}_{xx} + \tilde{\phi}_{xz}.$$

Thus, by integration by parts and using the fact that  $\tilde{\phi}(x, z, t)$  and its derivatives are assumed to be periodic in  $x$ , we have that

$$\begin{aligned} \int_{-L}^L g_M(x, \eta(x, t) + H, t) (1 + \eta_x^2)^{1/2} dx &= - \int_{-L}^L \left( \tilde{\phi}_z \psi_{M,j}^{(1)} + \tilde{\phi}_x \psi_{M,j}^{(2)} \right) \Big|_{z=\eta+H} dx \\ &\quad + \tilde{\phi}_z(L, \eta + H, t) \psi_{M,j}^{(\delta)}(\eta + H, t), \end{aligned}$$

where

$$\begin{aligned}\psi_{M,j}^{(1)}(x,t) &= \partial_x \psi_{M,j} + \eta_x \partial_z \psi_{M,j} \big|_{z=\eta+H}, \\ \psi_{M,j}^{(2)}(x,t) &= -\eta_x \partial_x \psi_{M,j} + \partial_z \psi_{M,j} \big|_{z=\eta+H}, \\ \psi_{M,j}^{(\delta)}(z,t) &= \psi_{M,j}(L,z,t) - \psi_{M,j}(-L,z,t).\end{aligned}$$

Likewise, we have that

$$\begin{aligned}\int_0^{\eta(L,t)+H} (g_M(L,z,t) + g_M(-L,z,t)) dz &= \int_0^{\eta(L,t)+H} \left( \tilde{\phi}_{xx}(L,z,t) \psi_{M,j}^{(\delta)}(z,t) \right. \\ &\quad \left. + \tilde{\phi}_x(L,z,t) \psi_{M,j}^{(\delta,x)}(z,t) \right) dz,\end{aligned}$$

where

$$\psi_{M,j}^{(\delta,x)}(z,t) = \partial_x \psi_{M,j}(L,z,t) - \partial_x \psi_{M,j}(-L,z,t).$$

One can readily show that

$$\psi_{M,j}^{(\delta)} = \frac{1}{4\pi} \ln \left( \left( \frac{(1 - \tilde{x}_j - 2M)^2 + \tilde{z}_{j,-}^2}{(1 - \tilde{x}_j + 2(M+1))^2 + \tilde{z}_{j,-}^2} \right) \left( \frac{(1 - \tilde{x}_j - 2M)^2 + \tilde{z}_{j,+}^2}{(1 - \tilde{x}_j + 2(M+1))^2 + \tilde{z}_{j,+}^2} \right) \right),$$

where

$$\tilde{x}_j = \frac{x_j}{L},$$

and thus

$$\lim_{M \rightarrow \infty} \psi_{M,j}^{(\delta)}(z,t) = 0.$$

Letting  $M \rightarrow \infty$ , we then have

$$\tilde{\phi}_x(x_j, z_j, t) = - \int_{-L}^L \left( \tilde{\phi}_z (\partial_x \psi_j + \eta_x \partial_z \psi_j) + \tilde{\phi}_x (-\eta_x \partial_x \psi_j + \partial_z \psi_j) \right) \big|_{z=\eta+H} dx,$$

where we define the functions  $\partial_x \psi_j$  and  $\partial_z \psi_j$  such that

$$\begin{aligned}\partial_x \psi_j(x, z, t) &= \lim_{M \rightarrow \infty} \partial_x \psi_{M,j}(x, z, t), \\ \partial_z \psi_j(x, z, t) &= \lim_{M \rightarrow \infty} \partial_z \psi_{M,j}(x, z, t).\end{aligned}$$

## 6.2 Potential Terms

The definition of the functions in Equations (13), (14), (15), and (16) are as follows:

$$\begin{aligned}\phi_{sz}(x,t) &= F \sum_{j=1}^N \Gamma_j \varphi_z(x - x_j, 1 + \mu\eta; z_j), \\ \phi_{sx}(x,t) &= F \sum_{j=1}^N \Gamma_j \varphi_x(x - x_j, 1 + \mu\eta; z_j),\end{aligned}$$

$$\begin{aligned}\varphi_z(x, z; z_j) &= \frac{\sin(\pi x) \sinh(\pi \gamma z) \sinh(\pi \gamma z_j)}{2 (\cosh(\pi \gamma (z - z_j)) - \cos(\pi x)) (\cosh(\pi \gamma (z + z_j)) - \cos(\pi x))}, \\ \tilde{\varphi}_z(x, z; z_j) &= \frac{\sin(\pi x) (\cosh(\pi \gamma z_j) \cosh(\pi \gamma z) - \cos(\pi x))}{2 (\cosh(\pi \gamma (z - z_j)) - \cos(\pi x)) (\cosh(\pi \gamma (z + z_j)) - \cos(\pi x))}, \\ \varphi_x(x, z; z_j) &= \frac{\sinh(\pi \gamma z_j) (\cosh(\pi \gamma z_j) - \cosh(\pi \gamma z) \cos(\pi x))}{2 (\cosh(\pi \gamma (z - z_j)) - \cos(\pi x)) (\cosh(\pi \gamma (z + z_j)) - \cos(\pi x))}, \\ \tilde{\varphi}_x(x, z; z_j) &= \frac{\sinh(\pi \gamma z) (\cosh(\pi \gamma z) - \cosh(\pi \gamma z_j) \cos(\pi x))}{2 (\cosh(\pi \gamma (z - z_j)) - \cos(\pi x)) (\cosh(\pi \gamma (z + z_j)) - \cos(\pi x))}.\end{aligned}$$

## References

- [1] M.J. Ablowitz, A.S. Fokas, and Z.H. Musslimani. On a new non-local formulation of water waves. *J. Fluid Mech.*, 562:313–343, 2006.
- [2] P.A. Tyvand. On the interaction between a strong vortex pair and a free surface. *Phys. Fluids A*, 2:1624–1634, 1990.
- [3] P.A. Tyvand. Motion of a vortex near a free surface. *J. Fluid Mech.*, 225:673–686, 1991.
- [4] S. Fish. Vortex dynamics in the presence of free surface waves. *Phys. Fluids A*, 3:504–506, 1991.
- [5] D.L. Marcus and S.A. Berger. The interaction between a counter-rotating vortex pair in vertical ascent and a free surface. *Phys. Fluids A*, 1:1988–2000, 1989.
- [6] J. G. Telste. Potential flow about two counter-rotating vortices approaching a free surface. *J. Fluid Mech.*, 201:259–278, 1989.
- [7] W.W. Willmarth, G. Tryggvason, A. Hirs, and D. Yu. Vortex pair generation and interaction with a free surface. *Phys. Fluids A*, 1:170–172, 1989.
- [8] E.A. Kuznetsov and V.P. Ruban. Cherenkov interaction of vortices with a free surface. *JETP*, 88:492–505, 1999.
- [9] W. Craig and C. Sulem. Numerical simulation of gravity waves. *J. Comput. Phys.*, 108:73–83, 1993.
- [10] P. Guyenne and D.P. Nicholls. A high-order spectral method for nonlinear water waves over moving bottom topography. *SIAM J. Sci. Comput.*, 30:81–101, 2007.
- [11] A. Rouhi and J. Wright. Hamiltonian formulation for the motion of vortices in the presence of a free surface for ideal flow. *Phys. Rev. E*, 48:1850–1865, 1993.
- [12] C. Lin, T.C. Ho, S.C. Chang, S.C. Hsieh, and K.A. Chang. Vortex shedding induced by a solitary wave propagating over a submerged vertical plate. *Int. J. Heat and Fluid Flow*, 26:894–904, 2005.

- [13] K.A. Chang, T.J. Hsu, and P.L.F. Liu. Vortex generation and evolution in water waves propagating over a submerged rectangular obstacle. Part I: Solitary waves. *Coast. Eng.*, 44:13–36, 2001.
- [14] K.A. Chang, T.J. Hsu, and P.L.F. Liu. Vortex generation and evolution in water waves propagating over a submerged rectangular obstacle. Part II: Cnoidal waves. *Coast. Eng.*, 52:257–283, 2005.
- [15] G.H. Cottet and P.D. Koumoutsakos. *Vortex Methods: Theory and Practice*. Cambridge University Press, Cambridge, 2000.
- [16] G. R. Baker and D. I. Meiron and S.A. Orszag. Generalized vortex methods for free-surface flow problems. *J. Fluid. Mech.*, 123,:477–501, 1982.
- [17] J. Wilkening and V. Vasan. Comparison of five methods of computing the Dirichlet–Neumann operator for the water wave problem. In *Nonlinear Wave Equations: Analytic and Computational Techniques*. AMS, 2015.
- [18] H. Lamb. *Hydrodynamics*. Dover, New York, N.Y., 1945.